# A Study of Ray-Chaotic Cylindrical Scatterers

Giuseppe Castaldi, Vincenzo Galdi, *Senior Member, IEEE*, and Innocenzo M. Pinto, *Senior Member, IEEE*

***Abstract*—Ray chaos, manifested by the exponential divergence of trajectories originating from an originally thin ray bundle, can occur even in linear electromagnetic propagation environments, due to the inherent nonlinearity of ray-tracing (eikonal) maps. In this paper, extending our previous study of a two-dimensional planar ray-chaotic prototype scenario, we consider a cylindrical scatterer made of a perfectly electric-conducting azimuthally corrugated boundary coated by a radially inhomogeneous (ray-trapping) dielectric layer. For this configuration, we carry out a comprehensive parametric study of the ray-dynamical and full-wave scattering (monostatic and bistatic radar-cross-section) signatures, with emphasis on possible implications for high-frequency wave asymptotics ("ray-chaotic footprints").**

***Index Terms*—High-frequency, radar cross-section, ray chaos.**

## I. Introduction

In CERTAIN *linear* and *deterministic* electromagnetic (EM) propagation/scattering scenarios, ray trajectories may become *exponentially sensitive* to small changes in the initial conditions, thereby exhibiting *long-range-unpredictable* dynamics. Remarkably, while this could intuitively be expected in very *complex* and *cluttered* propagation scenarios, it can also be observed in *deceptively simple* (but coordinate-nonseparable) structures that give rise to multiple reflections, focusing, and defocusing, such as "billiard-shaped" enclosures [1], [2], $(n > 3)$-disk "pinballs" [3], [4], or appropriately configured inhomogeneous refractive media with ray-trapping properties [5]. Such pathological behavior can be properly characterized within the framework of *deterministic chaos theory* [6], and is accordingly referred to as "ray chaos."

Perhaps the most immediate implication of ray chaos is of *computational* nature, and regards the possible hindering of numerical convergence (and, hence, applicability) of ray-based algorithms [7]. Less intuitive, but particularly intriguing, are the *phenomenological* implications, leading to the apparent paradox which stems from approximating, in the high-frequency (HF) regime, a *linear wave* equation (which does not exhibit exponential sensitivity to initial conditions in deterministic environments) in terms of a *nonlinear ray* equation that is prone to chaotic dynamics. In fact, although the *extremely complex* and *irregular* features of chaos are clearly incompatible with the inherently *smooth* character of wave dynamics, there is substantiated (theoretical, numerical, and experimental) evidence that the HF wave dynamics of ray-chaotically inclined systems exhibit distinctive "footprints" that are not observed in the case of "regular" (e.g., coordinate-separability-induced) ray behavior (see [8]–[10] for a review of known results, mostly developed within the framework of quantum physics). Besides the inherent academic interest, ray-chaotic manifestations have already been shown to play a major role in several engineering applications, ranging from reverberation enclosures to high-performance microlasers (see [10] for a recent review).

In an ongoing series of investigations [10], [11]–[17], we have focused on the wave-physical mechanisms that govern the tendency toward, and the onset of, ray-chaotic footprints in the HF/short-pulse regime of ray-chaotically inclined EM propagation/scattering scenarios. In particular, we explored in [13], [14], and [17] a 2-D planar ray-chaotic wave guiding/scattering *open* configuration, consisting of a planar stratified dielectric medium with exponentially tapered refractive index profile bounded by a smooth periodically corrugated perfectly electric-conducting (PEC) bottom surface, which constitutes the EM analog of a well-known gravitational billiard [5]. Results for the HF regime indicated trends toward irregularity and other anomalous characteristics interpretable as ray-chaotic footprints. In the irregular regime, the wave dynamics was found to be effectively described via *random-wave* statistical models similar to those in [8], [9], and possible applications to radar countermeasures and smart microwave absorbers were envisaged [14].

In order to gain further insight, in this paper, expanding upon previous preliminary results [15], [16], we extend the above analysis to a more interesting and realistic *cylindrical* version, whose *transversely finite* extent allows for characterization and assessment of the scattering signatures in terms of radar cross section (RCS). Interestingly, the combined effects of periodic azimuthal corrugations and *homogeneous* dielectric fillings in PEC cylindrical scatterers have already been explored (see, e.g., [18]) as a possible route for RCS reduction/control. It therefore appears suggestive to look at this configuration from a different (ray-chaos-motivated) perspective, which might offer new insights, also in view of the current advances in the synthesis of *spatially inhomogeneous* "metamaterials" (see, e.g., [19], [20]) which have recently led to previously inconceivable applications (see, e.g., [21]).

Accordingly, the rest of the paper is organized as follows. In Section II, we introduce the problem geometry. In Section III, we deal with its ray-dynamical properties, whereas, in Section IV, we address its full-wave study via a problem-matched semi-analytic technique (based on a generalized Fourier–Bessel expansion and adaptive point-matching), and present a parametric study of its RCS signatures aimed at ascertaining the possible presence of ray-chaotic footprints in the HF regime. Finally, in Section V, we summarize conclusions and hints for future research.

Manuscript received December 12, 2007; revised April 4, 2008. Published August 6, 2008 (projected).

The authors are with the Waves Group, Department of Engineering, University of Sannio, I-82100 Benevento, Italy (e-mail: castaldi@unisannio.it; vgaldi@unisannio.it, pinto@sa.infn.it).

Digital Object Identifier 10.1109/TAP.2008.927568

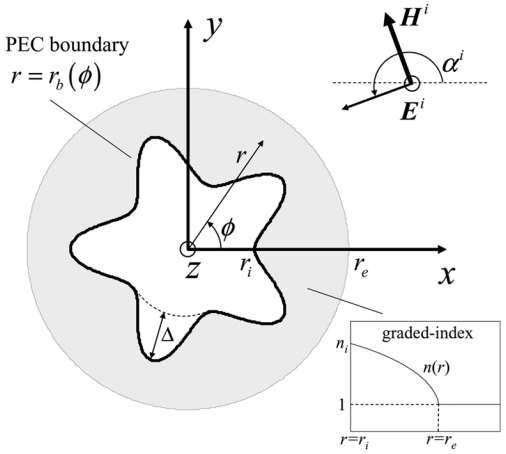


Fig. 1. Problem geometry: A PEC azimuthally periodic corrugated cylinder, parameterized by the polar curve $r = r_b(\phi)$ [oscillating between $r_i$ and $r_i + \Delta$, cf. (1)], is coated by a dielectric layer with a radially inhomogeneous refractive index profile $n(r)$ which is free-space-matched at $r = r_e > r_i + \Delta$ and increases with depth (cf. Fig. 2) up to a value $n_i$ at $r = r_i$ (see inset). Also shown are the Cartesian and cylindrical reference coordinate systems, and the E-polarized plane-wave excitation (with incidence angle $\alpha^i$ and $z$-directed electric field) considered in the full-wave analysis.

## II. Problem Geometry

Referring to the $(r, \phi, z)$ cylindrical coordinate system in Fig. 1, we consider a configuration composed of a $z$-independent smooth cylindrical PEC boundary with $N_p$ periodic azimuthal corrugations of peak-to-peak height $\Delta$, described by the profile

$$r_b(\phi) = \frac{2r_i(r_i + \Delta)}{2r_i + \Delta\,[1 + \cos(N_p\phi)]} \tag{1}$$

coated with a radially inhomogeneous (ray-trapping) refractive-index profile

$$n(r) = \sqrt{n_0^2 - \left(\frac{r}{\rho}\right)^2} \qquad n_0^2 = \frac{n_i^2 r_e^2 - r_i^2}{r_e^2 - r_i^2}$$
$$\rho = \sqrt{\frac{r_e^2 - r_i^2}{n_i^2 - 1}}. \tag{2}$$

The profile in (2) attains its maximum value $n_i$ on the interior boundary ($r = r_i$), and is free-space-matched and truncated at $r = r_e[n(r_e) = 1]$, with $r_e > r_i + \Delta$. Such profile has been judiciously selected so as to allow analytic solution of both the ray and Helmholtz equations in the unbounded medium. However, we highlight that the results presented hereafter are rather general, and depend on distinctive gross features of the corrugation (e.g., peak-to-peak height) and refractive-index (e.g., gradient) profiles, rather than on the particular parametric forms chosen.

## III. Ray Analysis

### A. Ray Tracing

Following [22] (see Appendix I for details), it can be shown that, in an unbounded medium with refractive index profile (2),

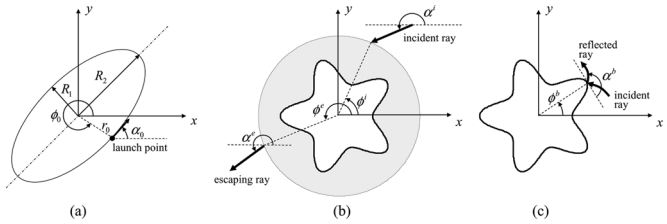


Fig. 2. Geometries relevant to the ray analysis. (a): Elliptical trajectory of a ray originating at $(r_0, \phi_0)$ with departure angle $\alpha_0$ in an unbounded medium with refractive-index profile as in (2). (b): Parameterization of incident/escaping rays via incidence/exit points ($\phi^i$ and $\phi^e$, respectively) and directions ($\alpha^i$ and $\alpha^e$, respectively). (c): Phase-space parameterization via impact-point position ($\phi^b$) and reflected-ray departure angle ($\alpha^b$).

the trajectory of a ray originating at $(r_0, \phi_0)$ with departure angle $\alpha_0$ (measured from the $x$-axis) is described by

$$r(\phi) = \left[\frac{\cos^2(\phi - \phi_0 + \psi)}{R_1^2} + \frac{\sin^2(\phi - \phi_0 + \psi)}{R_2^2}\right]^{-1/2} \tag{3}$$

where

$$R_{1,2} = \frac{u}{\sqrt{n_0^2 \pm \sqrt{v^2 + w^2}}} \tag{4a}$$
$$\psi = \frac{1}{2}\arctan\left(\frac{w}{v}\right) \tag{4b}$$

with

$$u = \sqrt{2} r_0 n(r_0) |\sin(\alpha_0 - \phi_0)| \tag{5a}$$
$$v = 2n^2(r_0)\sin^2(\alpha_0 - \phi_0) - n_0^2 \tag{5b}$$
$$w = n^2(r_0)\sin[2(\alpha_0 - \phi_0)]. \tag{5c}$$

Equation (3) defines a tilted ellipse centered at $(x = 0, y = 0)$ with semi-axes $R_1$ and $R_2 > R_1$ [see Fig. 2(a)]. In the configuration of interest, rays can be tracked analytically in the dielectric layer $r_b(\phi) < r < r_e$, whereas their interactions with the PEC boundary $r = r_b(\phi)$ and the free-space interface at $r = r_e$ need to be studied separately by solving (either numerically or analytically) the nonlinear equations arising from the local application of Snell's laws (see the discussion in [17], Section III-B, concerning the role of roundoff numerical errors).

### B. Representative Results

In order to select parametric configurations that could favor the onset of ray chaos, we preliminarily calculated the ray-launch position $\bar{r}_0$ on the PEC boundary that maximizes the distance between the ray turning-point and the free-space interface, i.e., that minimizes the major semi-axis $R_2$ in Fig. 2(a). After some algebra, this yields

$$\bar{r}_0 = \sqrt{\frac{n_i^2 r_e^2 - r_i^2}{2(n_i^2 - 1)}} \approx \frac{r_e}{\sqrt{2}}, \quad n_i \gg 1. \tag{6}$$

Accordingly, in all examples hereafter, we consider $r_e = \sqrt{2}(r_i + \Delta/2)$, which corresponds to placing the ray-launch position in (6) at midway between the corrugation extrema. Intuitively, this choice should provide, on average,

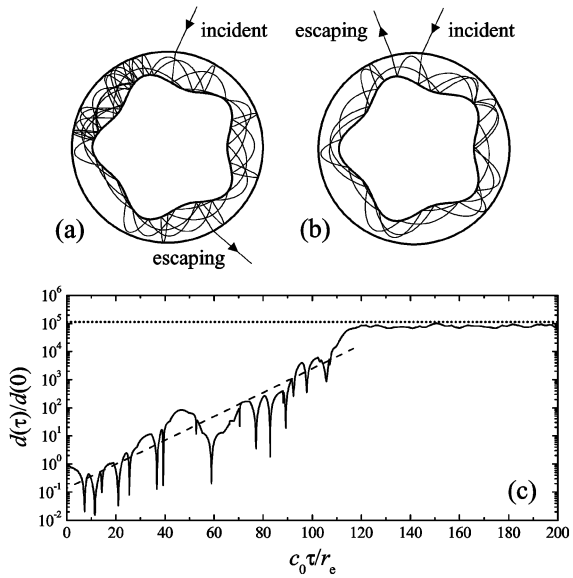


Fig. 3. Geometry as in Fig. 1, with $n_i = 15$, $r_e = \sqrt{2}(r_i + \Delta/2)$, $\Delta = r_i/4$, $N_p = 5$. Ray-tracing examples. (a), (b) Trajectories originating from two incident parallel ($\alpha^i = 245°$) rays with very close incidence positions ($\phi^i = 85°$ and $\phi^i = 84.999°$, respectively). (c) Separation $d$ between the above ray trajectories [scaled by its initial value $d(0)$] as a function of the "ray-time" $\tau$ in (8) (scaled by $c_0^{-1} r_e$). The initial *exponential* trend (typical of chaotic dynamics) is highlighted by the semi-log scale in the graph and the dashed linear fit. The dotted horizontal line represents the maximum separation $2r_e$ [scaled by $d(0)$] achievable inside the dielectric layer.

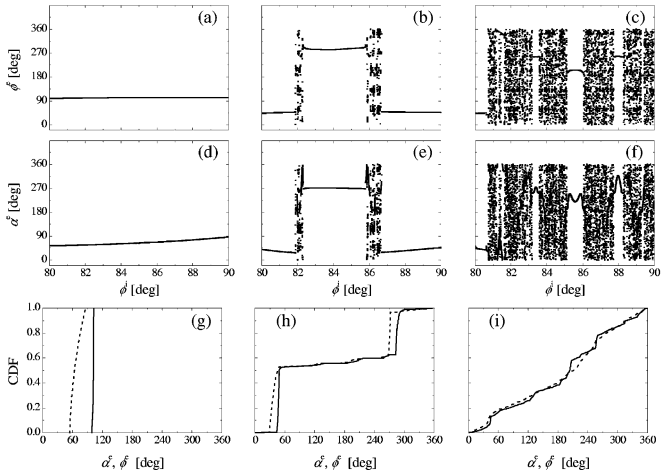


Fig. 4. As in Fig. 3, but exit maps and statistics for a bundle of $10^4$ parallel ($\alpha^i = 245°$) rays with incidence positions $\phi^i$ uniformly distributed within the interval $[80°, 90°]$, and different values of $n_i$. (a)–(c) Exit position $\phi^e$ as a function of $\phi^i$, for $n_i = 1$, 5, 15, respectively. (d)–(f) Exit direction $\alpha^e$ as a function of $\phi^i$, for $n_i = 1$, 5, 15, respectively. (g)–(i) Cumulative distribution functions (CDFs) of $\phi^e$ (continuous curves) and $\alpha^e$ (dashed curves), for $n_i = 1$, 5, 15, respectively.

good ray-trapping capabilities. In our simulations, incident and escaping rays are parameterized by the angles $\phi^i$, $\alpha^i$ and $\phi^e$, $\alpha^e$, which define, respectively, the position of the impact-point (modulo 360°) at the free-space interface and the incidence/departure directions [see Fig. 2(b)]. The multibounce ray dynamics inside the dielectric layer is parameterized via a typical phase-space diagram (impact map), displaying, for each encounter with the PEC boundary, the angular position $\phi^b$ of the impact point as a function of the cosine of the corresponding departure angle $\alpha^b$ with respect to the local tangent unit vector [see Fig. 2(c)]. As a further observable of interest, we also consider the so-called "dwell-time" (i.e., the time spent by the rays in the structure before escaping) [4]

$$\tau_D = c_0^{-1} \int_{r(s)<r_e} n(s) ds \tag{7}$$

with $c_0$ denoting the free-space wavespeed, and $s$ denoting the curvilinear abscissa.

Fig. 3(a) and (b) show the evolution of two typical ray trajectories, originating from nearly co-incident ($\phi^i = 85°$ and 84.999°, respectively) parallel ($\alpha^i = 245°$) rays, for a configuration featuring a strongly graded refractive-index profile ($n_i = 15$) and moderately deep corrugations ($N_p = 5$, $\Delta = r_i/4$). As they progress trough the structure, subject to multiple back–forth hops, the two initially indistinguishable ray trajectories spread widely, resulting in completely different exit positions and directions. This is better quantified in Fig. 3(c), which displays the (logarithm of the) ray reparation quantified by the distance $d$ between the two rays in Fig. 3 [normalized to its initial value $d(0)$] as a function of the "ray-time"

$$\tau = c_0^{-1} \int_{\text{ray path}} n(s) ds. \tag{8}$$

The semi-log scale used in the plot highlights the initial linear *exponential* trend typical of chaotic dynamics, with the slope (suitably averaged over the range of ray-launch conditions) providing an estimate of the Lyapounov exponent [6]. However, unlike in the transversely infinite planar configuration in [17], the ray separation inside the transversely finite cylindrical configuration of interest here is obviously bounded by the cylinder diameter $2r_e$, as clearly visible from Fig. 3(c). Note that different ray-separation metrics could be used, based, e.g., on the local "ray intensity" of a ray bundle (see [7] for details).

From a comprehensive set of ray-tracing simulations, typical results are shown in Figs. 4–7 in terms of the above-defined ray observables, for a thin bundle of $10^4$ parallel ($\alpha^i = 245°$) incident rays with incident positions $\phi^i$ uniformly distributed within the interval $[80°, 90°]$, and three representative values of the maximum refractive-index, varying from $n_i = 1$ (i.e., no coating) to $n_i = 15$ (strongly graded coating, cf. Fig. 3). Specifically, Fig. 4 shows the exit angle $\phi^e$ and direction $\alpha^e$ as a function of the incidence position $\phi^i$, as well as their cumulative distribution functions (CDFs). The configuration featuring $n_i = 1$ (i.e., PEC corrugated cylinder with no coating) exhibits *regular* exit-maps [cf. Fig. 4(a) and (d)], corresponding to rapidly escaping rays, and step-like CDFs [cf. Fig. 4(g)]. Increasing the maximum refractive-index to $n_i = 5$, one observes the appearance of regions of irregularity (corresponding to multibounce-trapped, exponentially diverging rays) in the exit-maps [cf. Fig. 4(b) and (e)], with a corresponding multistep behavior of the CDFs. Finally, for the strongly graded profile ($n_i = 15$), the regions of irregularity tend to become dominant [cf.

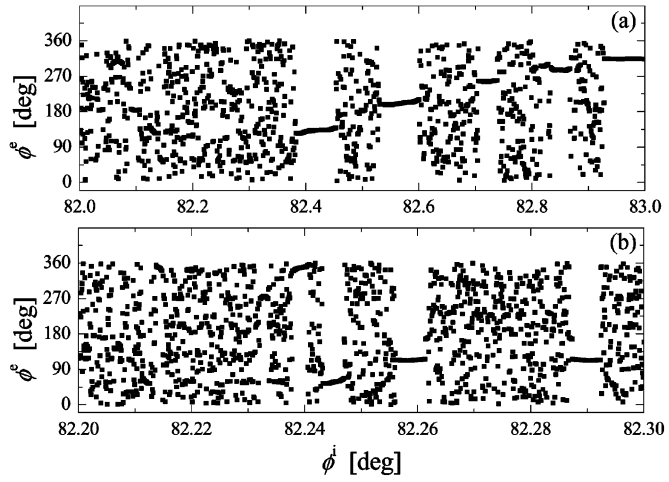


Fig. 5. Magnified details of Fig. 4(c), displaying the intermingled regular/irregular structure at subscales of the incidence-position interval. (a) $\phi^i \in [82°, 83°]$ (i.e., 1/10 scale). (b) $\phi^i \in [82.2°, 82.3°]$ (i.e., 1/100 scale).

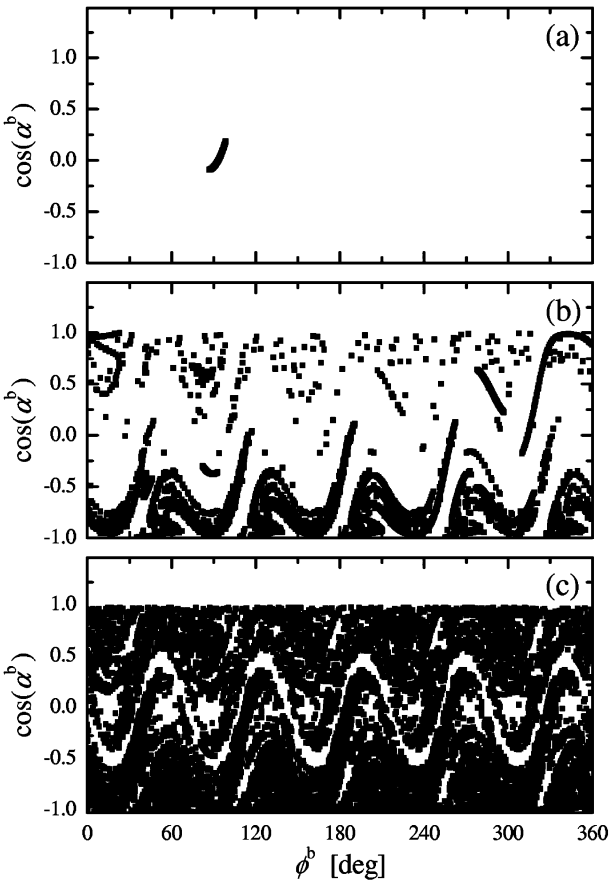


Fig. 6. As in Fig. 4, but impact maps [cf. Fig. 2(c)]. (a)–(c) $n_i = 1, 5, 15$, respectively.

Fig. 4(c) and (f)], and the CDFs tend to become nearly linear (corresponding to nearly uniform statistical distributions). As typical in open billiards, the intermingled regular/irregular dependence on the incidence position can actually be observed at *arbitrarily small* scales (see, e.g., [4] for details about its *fractal* nature), as shown in Fig. 5 with reference to the exit-position map.

Fig. 6 shows the corresponding impact maps [$\cos(\alpha^b)$ as a function of $\phi^b$, cf. Fig. 2(c)]. As the maximum-refractive index is increased, one observes the phase-space to become progressively filled-up, and asymptotically covered *uniformly*, with possible exceptions of "regular islands" (corresponding to, e.g., marginally stable periodic trajectories).

Finally, Fig. 7 shows the dwell-time complementary CDFs. As the maximum refractive-index is increased, one observes a tendency from a staircase-type toward a linear *exponential* behavior [cf. Fig. 7(c)], as evidenced by the semi-log scale utilized. As discussed in [4], the parameters of this CDF are strongly tied with the ray-dynamical Lyapounov exponent and the above-observed fractal characteristics of the exit maps.

Results similar to the above were consistently observed within a broad range of incidence parameters. Also, similar trends toward irregular ray-dynamics (not shown here for brevity) were observed, for fixed refractive-index profiles, by increasing the peak-to-peak corrugation height from $\Delta = 0$ (i.e., circular PEC cylinder) to the value $\Delta = r_i/4$ utilized in the above examples.

*Remarks*

To sum up, in the cylindrical configuration of interest here, the ray dynamics turns out to be generally "mixed," entailing the presence of both regular and irregular regions in the phase space. Results clearly indicate the existence of parametric ranges that favor the dominance of irregular dynamics. In this regime:

- rays tend to be trapped, executing many back–forth hops before escaping;
- nearly co-incident rays spread *exponentially* [with possible saturation, cf. Fig. 3(c)].;
- rays originating from compact incident bundles exhibit nearly *uniformly distributed* exit angles and directions, with intermingled regular/irregular dependence on the incidence parameters at arbitrarily small scales, and nearly *exponentially distributed* dwell-times (see also the discussion in [17], Section III-B, concerning the possible presence of *power-law* tails in the mixed regime).

The above results represent typical indicators of ray chaos, also observed in different ray-chaotic scattering configurations [4], [10], [17].

## IV. Full-Wave Analysis

We consider a time-harmonic $[\exp(j\omega t)]$ unit–amplitude incident plane-wave with $z$-polarized electric field (see Fig. 1), which can be conveniently expanded into a Fourier–Bessel series

$$E^i(r,\phi) = \exp\left[-jk_0\left(x\cos\alpha^i + y\sin\alpha^i\right)\right] = \sum_{m=-\infty}^{\infty} J_m(k_0 r)\exp\left[jm\left(\phi - \alpha^i - \frac{\pi}{2}\right)\right] \quad (9)$$

with $k_0 = \omega\sqrt{\epsilon_0\mu_0}$ denoting the free-space wavenumber, and $J_m$ the $m$th-order Bessel function of first kind [23, Chap. 9]. In (9), and henceforth, the explicit dependence on $k_0$ is omitted, unless strictly needed.

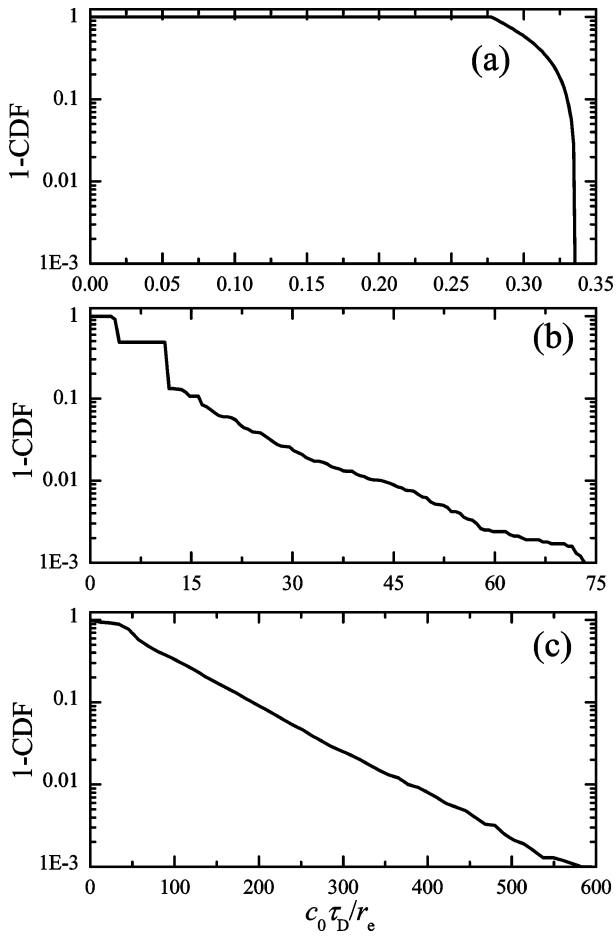


Fig. 7. As in Fig. 6, but complementary CDF (i.e., 1-CDF) of dwell-time $\tau_D$ in (7) (scaled by $c_0^{-1}r_e$).

### A. Method

As in [17], we developed a problem-matched semi-analytic technique. In order to reduce the computational burden, in view of the azimuthal periodicity of the structure, it is expedient to recast the Fourier–Bessel expansion in (9) as

$$E^i(r,\phi) = \sum_{p=0}^{N_p-1} E_p^i(r,\phi) \tag{10}$$

where

$$E_p^i(r,\phi) = \sum_{m=-\infty}^{\infty} J_{m_p}(k_0 r)\exp\left[jm_p\left(\phi-\alpha^i-\frac{\pi}{2}\right)\right] \tag{11}$$

and $m_p = p + mN_p$. Accordingly, exploiting the linearity of the problem, we solve a number $N_p$ of EM problems corresponding to excitations $E_p^i(r,\phi)$, $p = 1,\ldots,N_p$, whose azimuthal periodicity (of period $360^\circ/N_p$) exactly matches that of the corrugated PEC boundary in (1). The scattered field $E^s$ in the free-space region $(r > r_e)$ and the transmitted field $E^t$ into the dielectric layer $[r_b(\phi) < r < r_e]$ are likewise expanded into this type of series, synthesized in terms of radial wavefunctions which satisfy the relevant Helmholtz equations

$$E_p^s(r,\phi) = \sum_{m=-\infty}^{\infty} c_{m_p} H_{m_p}^{(2)}(k_0 r)\exp(jm_p\phi), \tag{12}$$

$$E_p^t(r,\phi) = \sum_{m=-\infty}^{\infty}\left[a_{m_p}F_{m_p}^{(1)}(k_0 r) + b_{m_p}F_{m_p}^{(2)}(k_0 r)\right] \times \exp(jm_p\phi). \tag{13}$$

In (12) and (13), $a_{m_p}$, $b_{m_p}$, and $c_{m_p}$ are unknown coefficients, and $H_m^{(2)}$ denotes the $m$th-order Hankel function of the second kind [23, Eq. (9.1.14)], in accord with the radiation condition at $r \to \infty$, whereas $F_m^{(1,2)}$ denote independent solutions of the radial Helmholtz equations inside the dielectric layer

$$\left[\frac{1}{r}\frac{d}{dr}\left(r\frac{d}{dr}\right) + k_0^2 n^2(r) - \frac{m^2}{r^2}\right] F_m(k_0 r) = 0. \tag{14}$$

It can be shown (see Appendix II for details) that, for the refractive-index profile in (2), these solutions can be written as

$$F_m^{(1,2)}(k_0 r) = C_{1,2}\,(k_0 r)^{|m|}\exp\left(-\frac{\gamma k_0^2 r^2}{2}\right) \times \left\{\begin{array}{c} M\left(\nu,|m|+1,\gamma k_0^2 r^2\right) \\ U\left(\nu,|m|+1,\gamma k_0^2 r^2\right)\end{array}\right\} \tag{15}$$

where

$$\gamma = \frac{1}{k_0\rho}, \quad \nu = \frac{|m|+1}{2} - \frac{n_0^2 k_0\rho}{4} \tag{16}$$

and $M(a,b,z)$ and $U(a,b,z)$ are confluent hypergeometric functions (see, e.g., [23, Eqs. (13.1.2) and (13.1.3)]). Moreover, for convenience, the normalization constants $C_{1,2}$ are chosen so that $F_m^{(1,2)}(k_0 r_e) = 1$. The unknown expansion coefficients $a_{m_p}$, $b_{m_p}$, $c_{m_p}$ can be computed by enforcing the boundary conditions at the interfaces $r = r_e$ (continuity of the tangential components of the electric and magnetic field) and $r = r_b(\phi)$ (vanishing of the tangential component of the electric field)

$$E_p^t\left(r_e^-,\phi\right) = E_p^s\left(r_e^+,\phi\right) + E_p^i\left(r_e^+,\phi\right) \tag{17a}$$

$$\frac{\partial}{\partial r}E_p^t\left(r_e^-,\phi\right) = \frac{\partial}{\partial r}E_p^s\left(r_e^+,\phi\right) + \frac{\partial}{\partial r}E_p^i\left(r_e^+,\phi\right) \tag{17b}$$

$$E_p^t\left[r_b(\phi),\phi\right] = 0. \tag{17c}$$

By substituting the expansions (11)–(13) in the boundary conditions (17a) and (17b), we obtain in a straightforward fashion a doubly countable infinity of linear equations, from which two sets of unknown coefficients (say $a_{m_p}$ and $c_{m_p}$) can be expressed in terms of the remaining set ($b_{m_p}$), viz.

$$a_{m_p} = -\exp\left[-jm_p\left(\alpha^i+\frac{\pi}{2}\right)\right]\frac{W_{\left[H_{m_p}^{(2)},J_{m_p}\right]}}{W_{\left[H_{m_p}^{(2)},F_{m_p}^{(1)}\right]}} - b_{m_p}\frac{W_{\left[H_{m_p}^{(2)},F_{m_p}^{(2)}\right]}}{W_{\left[H_{m_p}^{(2)},F_{m_p}^{(1)}\right]}} \tag{18a}$$

$$c_{m_p} = \exp\left[-jm_p\left(\alpha^i + \frac{\pi}{2}\right)\right] \frac{W_{\left[J_{m_p}, F^{(1)}_{m_p}\right]}}{W_{\left[H^{(2)}_{m_p}, F^{(1)}_{m_p}\right]}} - b_{m_p} \frac{W_{\left[F^{(2)}_{m_p}, F^{(1)}_{m_p}\right]}}{W_{\left[H^{(2)}_{m_p}, F^{(1)}_{m_p}\right]}}. \quad (18b)$$

In (18), $W_{[f,g]}$ represents the Wronskian of the functions $f$ and $g$ evaluated at $k_0 r_e$

$$W_{[f,g]} = f(k_0 r_e)\, g'(k_0 r_e) - f'(k_0 r_e)\, g(k_0 r_e) \quad (19)$$

with $'$ denoting differentiation with respect to the argument. Then, letting (18a) in the more involved boundary condition (17c), we obtain

$$\sum_{m=-\infty}^{\infty} b_{m_p} F^{(2)}_{m_p}[k_0 r_b(\phi)]\left[1 - \Lambda_{m_p}(\phi)\right] \exp(jm_p\phi) = G_p(\phi) \quad (20)$$

where

$$\Lambda_{m_p}(\phi) = \frac{W_{\left[H^{(2)}_{m_p}, F^{(2)}_{m_p}\right]} F^{(1)}_{m_p}[k_0 r_b(\phi)]}{W_{\left[H^{(2)}_{m_p}, F^{(1)}_{m_p}\right]} F^{(2)}_{m_p}[k_0 r_b(\phi)]} \quad (21)$$

and

$$G_p(\phi) = -\sum_{m=-\infty}^{\infty} \frac{W_{\left[H^{(2)}_{m_p}, J_{m_p}\right]}}{W_{\left[H^{(2)}_{m_p}, F^{(1)}_{m_p}\right]}} F^{(2)}_{m_p}[k_0 r_b(\phi)] \times \exp\left[jm_p\left(\phi - \alpha^i - \frac{\pi}{2}\right)\right]. \quad (22)$$

A widely used numerical solution strategy consists of truncating the expansions in (20) to $|m| \le M_p$, and computing the surviving $2M_p + 1$ coefficients $b_{m_p}$ via point-matching (collocation), i.e., enforcing (20) in a set of $2M_p + 1$ matching-points on the PEC boundary $r = r_b(\phi)$. However, it is well known that numerical convergence may be *nonuniform* and strongly dependent on the choice of the matching-points [24]. In our implementation, we developed an *adaptive* point-matching strategy based on the framework developed in [24], which yields uniform convergence. The reader is referred to Appendix III for theoretical and implementation details.

### B. Representative Results

*1) Simulation Parameters and Preliminary Tests:* In all simulations below, we consider the same parametric ranges as in the ray-tracing analysis (Section III-B). Concerning the truncation of (20), from spatial-bandwidth considerations [25], we use the following estimate

$$M_p = \chi \frac{n_i k_0 L_b}{2\pi N_p} \quad (23)$$

with $L_b$ denoting the total length of the boundary $r = r_b(\phi)$, and $\chi$ being an excess-bandwidth factor (chosen as 1.8 in the numerical simulations). Fig. 8 compares the residual error (normalized, in view of the unit–amplitude excitation) in the boundary condition (17c) arising from the adaptive and uniform point-matching strategies, for a parameter configuration featuring a maximum refractive-index $n_i = 15$, $N_p = 5$ corrugations of peak-to-peak height $\Delta = r_i/8$, normalized frequency $k_0 r_e = 10$, and truncation index $M_p = 39$ [from (23)]. It is observed that our adaptive point-matching strategy yields a residual error always $< 10^{-5}$, whereas the one arising from uniform point-matching can be as large as $\sim 0.1$. This clearly illustrates the reliability of the proposed approach. As a further convergence test, we verified that the energy balance criterion [26] was satisfied to within $10^{-3}$ over a broad parametric range.

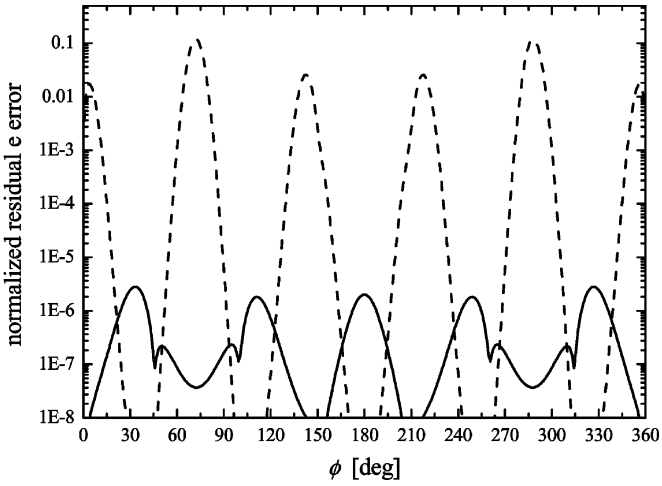


Fig. 8. Parameters as in Fig. 3, but with $\Delta = r_i/8$. Normalized residual error (absolute value) in the boundary condition (17c) arising from adaptive (continuous curve) and uniform (dashed curve) point-matching, for plane-wave incidence with $\alpha^i = 180^\circ$ and $k_0 r_e = 10$, and truncation index $M_p = 39$. Errors are evaluated at midpoints between two consecutive matching points.

*2) RCS Analysis:* As a meaningful observable to characterize the scattering signatures of the configuration under study, we consider the 2-D radar cross-section (RCS)

$$\sigma_{2D}(\phi, k_0) = \lim_{r\to\infty} 2\pi r |E^s(r, \phi; k_0)|^2 \quad (24)$$

with the $k_0$-dependence now explicitly indicated. From a comprehensive set of parametric studies, we illustrate below a body of representative results.

Fig. 9 shows the *monostatic* (i.e., observed at backscattering direction $\phi = \alpha^i - 180^\circ$, cf. Fig. 1) RCS response, for fixed incidence angle ($\alpha^i = 180^\circ$) and various parametric configurations (including those analyzed in Section III-B) ranging from regular to chaotic ray dynamics, within a frequency range extending up to an electrical size $k_0 r_e = 10$ (compatible with our current computational resources). Starting from the fairly regular response of a plain circular cylinder [Fig. 9(a)], it is observed how introducing *either* corrugations *or* graded-index-coating *alone* (i.e., preserving the ray-regular behavior) produces only smooth changes [Fig. 9(b)] or the appearance of isolated peaks [Fig. 9(c) and (e)]. Conversely, introducing *both* corrugation and graded-index-coating (which are *both* required for the onset of ray-chaos) produces increasingly complex RCS responses [Fig. 9(d) and (f)]. In particular, the configuration featuring $n_i = 15$ and $\Delta = r_i/4$, whose ray-chaotic dynamics was clearly illustrated in Section III-B [see Figs. 4(c), (f), and (i), 5, 6(b), and

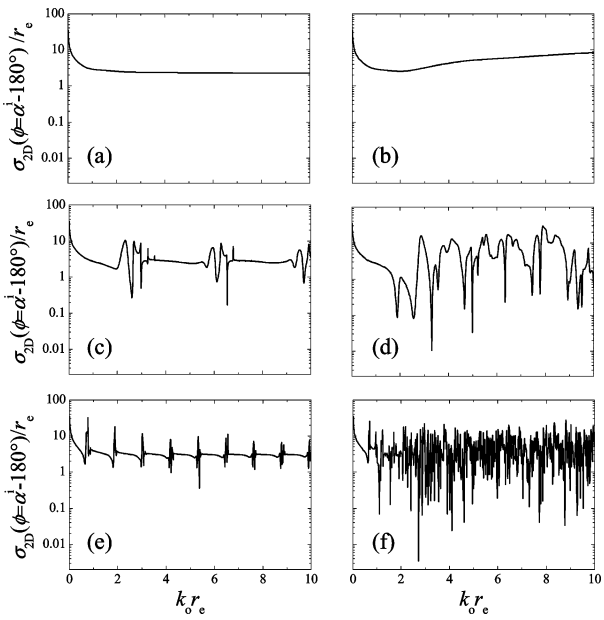


Fig. 9. Parameters as in Fig. 3, but (normalized) monostatic RCS as a function of normalized frequency $k_0 r_e$, for various values of $n_i$ and $\Delta$ corresponding to parametric configurations ranging from ray-regular to ray-chaotic behavior. The truncation index $M_p$ is chosen according to (23). (a) $n_i = 1, \Delta = 0$ (uncoated circular cylinder, ray-regular). (b) $n_i = 1$, $\Delta = r_i/4$ [uncoated corrugated cylinder, ray-regular, cf. Fig. 4(a), (d), and (g)]. (c) $n_i = 5, \Delta = 0$ (coated circular cylinder, ray-regular). (d) $n_i = 5, \Delta = r_i/4$ [coated corrugated cylinder, mainly regular ray dynamics, cf. Fig. 4(b), (e), and (h)]. (e) $n_i = 15, \Delta = 0$ (coated circular cylinder, ray-regular). (f) $n_i = 15, \Delta = r_i/4$ [coated corrugated cylinder, ray-chaotic, cf. Fig. 4(c), (f), and (i)].

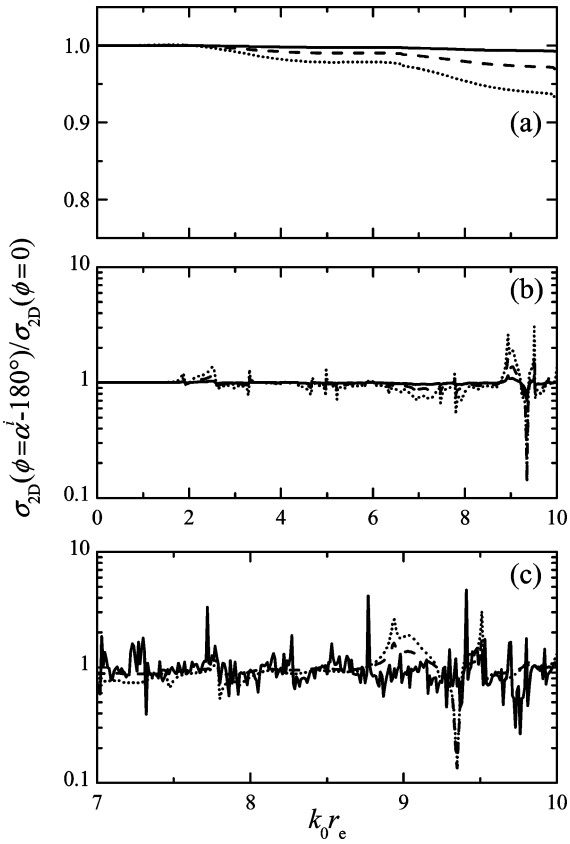


Fig. 10. As in Fig. 9(b), (d), and (f), but for various incidence angles. To better highlight possible variations, results are scaled to the $\alpha^i = 180°$ reference cases in Fig. 9(b), (d), and (f). (a) $n_i = 1, \Delta = r_i/4$.(b) $n_i = 5, \Delta = r_i/4$; (c): $n_i = 15, \Delta = r_i/4$ (for the sake of readability, only the higher frequency region is shown). Continuous curve: $\alpha^i = 181°$; dashed: $\alpha^i = 182°$; dotted: $\alpha^i = 183°$.

7(c)], exhibits a monostatic RCS response [see Fig. 9(f)] with very rapid and irregular frequency variations, and wide (up to three orders of magnitude) dynamic ranges. Such a response is typical for ray systems with mixed phase-space featuring large Kolmogorov–Arnold–Moser (KAM) islands, and the resonance spacing can be related to the winding ratio of the important KAM islands (see [27]–[29] for details).

For three representative parametric configurations from the above set, Fig. 10 illustrates the dependence of the monostatic RCS response on the incidence angle. To better visualize possible variations, the response for three nearby incidence angles ($\alpha^i = 181°, 182°, 183°$) are scaled to the previously shown response for $\alpha^i = 180°$ (extracted from Fig. 9). Again, ray-regular configurations [Fig. 10(a)] are observed to exhibit weak and smooth variations, whereas ray-chaotically inclined configurations, increasing the refractive-index gradient from mild [$n_i = 5$, cf. Fig. 10(b)] to strong [$n_i = 15$, cf. Fig. 10(c)] values, display increasingly stronger and irregular variations in the HF regime.

In order to gain a deeper insight into the angular distribution of the scattered power, Fig. 11 shows the *bistatic* RCS, for the same parametric configurations in Fig. 10 and fixed incidence direction, in a tiny neighborhood $(\pm 0.1 k_0 r_e)$ of three representative frequencies. It is observed that, for the ray-regular configuration [Fig. 11(a)–(c)], small frequency variations yield practically undistinguishable responses, across the whole frequency observation range. For ray-chaotically inclined configurations with a mild refractive-index gradient [Fig. 11(d)–(f)], only a mild frequency-sensitivity is observed for the larger electrical sizes. Increasing the refractive-index value [Fig. 11(g)–(i)], the frequency-sensitivity at the larger electrical sizes becomes significant across the whole angular range. This is better quantified in Fig. 12, which displays the normalized frequency-sensitivity indicator

$$\Delta\sigma_{2D}(k_0) = \frac{\int_0^{2\pi} |\sigma_{2D}(k_0 + \Delta k_0, \phi) - \sigma_{2D}(k_0, \phi)|^2 d\phi}{\int_0^{2\pi} |\sigma_{2D}(k_0, \phi)|^2 d\phi} \tag{25}$$

for the three parametric configurations of Fig. 11 (with $\Delta k_0 r_e = 0.1$). One observes the sensitivity to progressively grow from rather small values ($\Delta\sigma_{2D} \lesssim 10^{-2}$) for the ray-regular configuration [Fig. 12(a)] up to significantly larger values ($\Delta\sigma_{2D} \gtrsim 1$) for the strongly graded ray-chaotic configuration [Fig. 12(c)].

*Remarks*

To sum up, the above results clearly indicate that electrically large ray-chaotically inclined configurations exhibit fairly complex monostatic and bistatic RCS responses, characterized by wide dynamic ranges and strong sensitivity on the frequency and incidence direction, which are fairly different from those observed in ray-regular configurations. The ray-chaotic footprints observed in the high-frequency wave dynamics of the planar

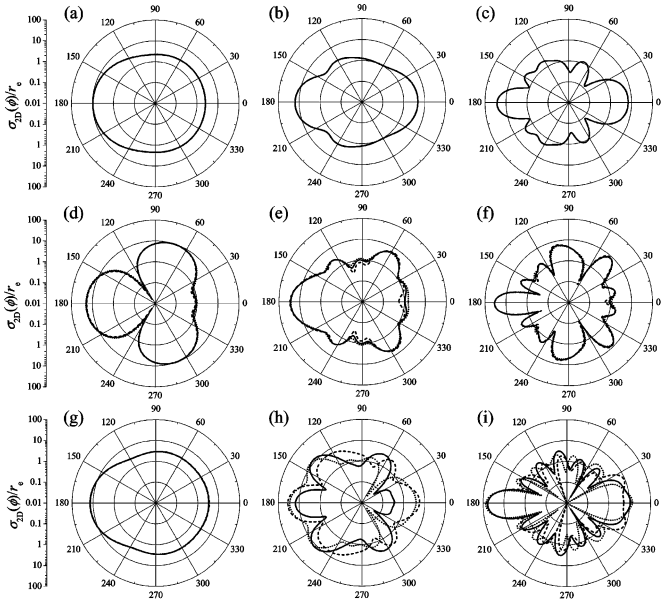


Fig. 11. As in Fig. 10, but bistatic RCS at three representative frequencies (continuous curves) and nearby values ($\pm 0.1 k_0 r_e$, dashed and dotted curves, respectively), for $\alpha^i = 180°$. (a)–(c) $n_i = 1$, $\Delta = r_i/4$ ($k_0 r_e = 2$, 5, 10, respectively; results at nearby frequencies are practically indistinguishable on the plot scale). (d)–(e) $n_i = 5$, $\Delta = r_i/4$ ($k_0 r_e = 2$, 5, 10, respectively). (g)–(i) $n_i = 15$, $\Delta = r_i/4$ ($k_0 r_e = 2$, 5, 10, respectively).

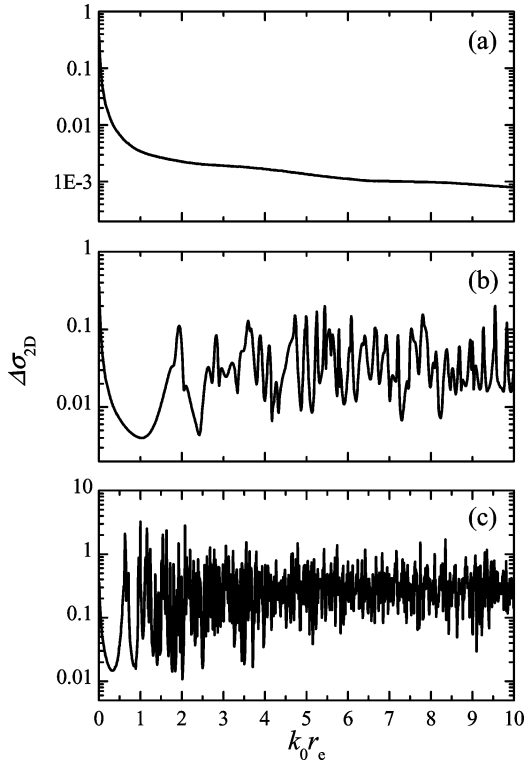


Fig. 12. As in Fig. 10, but normalized frequency-sensitivity indicator in (25) for $\alpha^i = 180°$.

(transversely infinite) scenario in [17] seem therefore to hold also for the more realistic cylindrical scatterers of interest here.

## V. Conclusion and Outlook

In this paper, extending our previous studies on planar geometries [17], we presented a prototype study of the ray-dynamics and wave-scattering properties of a class of ray-chaos-inclined 2-D cylindrical configurations, consisting of azimuthally corrugated PEC cylinders coated by radially inhomogeneous dielectric layers.

The ray-tracing analysis shows the existence of parametric ranges (for sufficiently high refractive-index gradients and corrugation heights) for which the ray dynamics is dominated by a strongly irregular behavior, which exhibits the typical hallmarks of chaos. The full-wave parametric studies of the scattering properties show that, in the above ray-chaotic parametric ranges, the HF wave dynamics also exhibits a tendency toward irregularity, which is not observed in ray-regular configurations. Ray-chaotic footprints are manifested, in the RCS signatures, by a strong sensitivity to frequency and incidence direction changes. Also observed in our prototype example is an increased dynamical range from ray-regular to ray-chaotic parameter configurations. However, its interpretation as a ray-chaotic footprint may be questionable, as such effects can also be observed in many different ray-regular scenarios under appropriate parameter configurations.

This prototype study sets the stage for a variety of follow-up investigations. In view of its easily *tunable* (from regular to chaotic) ray-dynamics and reference full-wave solution developed, it constitutes an interesting testbed for validation and calibration of problem-matched asymptotic high-frequency parameterizations, as well as for assessment of the effects of ray-chaos in the numerical convergence of ray-based algorithms. We are currently exploring hybrid ray-mode representations [30] and local spectral analysis [31], for shedding further light on the underlying phenomenologies and their interplay. In this connection, of great theoretical interest would be the study of the topological structure of the chaotic invariant set and the corresponding symbolic dynamics [32], and of their footprints in the wave dynamics, as well as the study of diffusive behavior and localization phenomena typical of "rough billiards" [33].

Another interesting area is the study of effective statistical representations of the wavefields in the irregular regime, and their connections with ray-dynamical observables [4]. In this framework, we are currently pursuing the optimization of our full-wave numerical code (presently written in Mathematica [34]) for greater efficiency, so as to afford a comprehensive statistical analysis of the scattering signatures. Moreover, particularly intriguing from the application viewpoint is the possible exploitation of the inherent richness and complexity of the RCS signatures of ray-chaotic scatterers in radar-countermeasure scenarios. In this connection, it is worth observing that the HF RCS response of ray-chaotic systems closely resembles (at least within the first-order statistics) those of irregular (e.g., rough) *incoherent* scatterers. Clearly, crucial for application purposes is a metamaterial-based implementation of the required graded-index profile, which could be pursued along the lines of the approaches in [19]–[21]. Also worth of interest are the study of the complex resonances (in a singularity-expansion-method framework) and their connections with the phase-space structure [27]–[29], as well as the extension to full 3-D (vector) configurations aimed at characterizing the (de)polarization response.

## APPENDIX I
## RAY EQUATION

From [22], the ray equation in a 2-D scenario featuring a radially inhomogeneous refractive-index profile $n(r)$ can be written, in cylindrical coordinates, as 8–

$$\frac{d\phi}{dr} = \frac{h}{r\sqrt{n^2(r)r^2 - h^2}} \tag{26}$$

where $h$ is a constant dependent on the ray-launch conditions. For the profile in (2), the ray equation in (26) admits the following closed-form solution:

$$\phi(r) = \phi_0 - \frac{1}{2}\arcsin\left[\frac{\rho\left(2h^2 - n_0^2 r^2\right)}{r^2\sqrt{n_0^4\rho^2 - 4h^2}}\right] + \frac{1}{2}\arcsin\left[\frac{\rho\left(2h^2 - n_0^2 r_0^2\right)}{r_0^2\sqrt{n_0^4\rho^2 - 4h^2}}\right] \tag{27}$$

where $\phi_0 = \phi(r_0)$ is determined by the ray-launch position. The ray trajectory in (3) is finally obtained by inverting (27) with respect to $r$, and enforcing the remaining condition on the ray departure angle $\alpha_0$

$$\tan\alpha_0 = \left.\frac{\frac{dy}{dr}}{\frac{dx}{dr}}\right|_{r=r_0} = \left.\frac{\frac{d(r\sin\phi)}{dr}}{\frac{d(r\cos\phi)}{dr}}\right|_{r=r_0} \tag{28}$$

which yields

$$h = r_0 n(r_0)\left|\sin(\alpha_0 - \phi_0)\right|. \tag{29}$$

## APPENDIX II
## PERTAINING TO (15)

Under the transformation $k_0 r^2 = \zeta\rho$, the radial Helmholtz equation in (14), with the refractive index profile in (2), can be recast as

$$\left[\frac{1}{\zeta}\frac{d}{d\zeta}\left(\zeta\frac{d}{d\zeta}\right) + \left(\frac{k_0\rho n_0^2}{4\zeta} - \frac{1}{4} - \frac{m^2}{\zeta^2}\right)\right] F_m\left(\frac{\rho\zeta}{r}\right) = 0 \tag{30}$$

which, via the mapping

$$F_m\left(\frac{\rho\zeta}{r}\right) = \zeta^{|m|/2}\exp\left(-\frac{\zeta}{2}\right)\bar{F}_m(\zeta) \tag{31}$$

can be reduced to the Kummer's equation [23, Eq. (13.1.1)]

$$\left[\zeta\frac{d^2}{d\zeta^2} + (|m| + 1 - \zeta)\frac{d}{d\zeta} - \frac{(|m|+1)}{2} + \frac{n_0^2\rho k_0}{4}\right]\bar{F}_m(\zeta) = 0. \tag{32}$$

Equation (32) admits two independent solutions in terms of confluent hypergeometric functions [23, Eqs. (13.1.2), (13.1.3)], from which the final solutions in (15) immediately follow via inverse mapping. Alternatively, via a different mapping in (31) [$F_m(\rho\zeta/r) = \zeta^{-1/2}\bar{F}_m(\zeta)$], (30) can be reduced to the Whittaker's equation (see, e.g., [23, Eq.(13.1.31)]).

## APPENDIX III
## ADAPTIVE POINT-MATCHING SCHEME

In this Appendix, we sketch the adaptive point-matching procedure utilized in our full-wave solution, referring to the appropriate references for details. Following [24], we exploit the large-order asymptotic expansions of the Bessel and Hankel functions [23, Eq. (9.3.1)]

$$J_m(k_0 r) \sim \frac{\exp(|m|)}{\sqrt{2\pi|m|}}\left(\frac{k_0 r}{2|m|}\right)^{|m|}, \qquad |m| \gg 1 \tag{33a}$$

and

$$H_m^{(2)}(k_0 r) \sim \frac{2j\exp(-|m|)}{\sqrt{2\pi|m|}}\left(\frac{k_0 r}{2|m|}\right)^{-|m|}, \qquad |m| \gg 1 \tag{33b}$$

as well as those for the confluent hypergeometric functions [23, Eqs. (13.5.13), (13.5.15)], from which [also in view of the choice of the normalization constants $C_{1,2}$ in (15)] it follows that

$$F_m^{(1,2)} \sim \left(\frac{r}{r_e}\right)^{\pm|m|}, \quad |m| \gg 1. \tag{33c}$$

By substituting in (20) the asymptotic expansions in (33), and recalling that $r_b < r_e$ (see Fig. 1), it can be shown that $\Lambda_{m_p}(\phi)$ asymptotically vanishes, yielding

$$\sum_{m=0}^{\infty} b_{p+mN_p}\left[\frac{r_b(\phi)}{r_e\exp(j\phi)}\right]^{-p-mN_p} + \sum_{m=1}^{\infty} b_{p-mN_p}\left[\frac{r_b(\phi)}{r_e\exp(-j\phi)}\right]^{p-mN_p} \approx G_p(\phi). \tag{34}$$

Next, by introducing the auxiliary complex mapping

$$\xi = \frac{r_e}{r}\exp(j\phi) \tag{35}$$

and indicating with $\Gamma_c$ the contour in the complex $\xi$-plane corresponding to the image of the boundary $r = r_b(\phi)$, (34) can be rewritten as

$$\sum_{m=0}^{\infty} b_{p+mN_p}\xi^{p+mN_p} + \sum_{m=1}^{\infty} b_{p-mN_p}(\xi^*)^{-p+mN_p} \approx \bar{G}_p(\xi), \quad \xi \in \Gamma_c \tag{36}$$

where $^*$ denotes complex conjugation, and $\bar{G}_p(\xi) = G_p[-j\log(\xi r/r_e)]$. Recalling the Riemann mapping theorem [35], there exists a unique conformal transformation

$$\eta = P(\xi) = \xi\sum_{k=0}^{\infty} p_k\xi^{-kN_p}, \quad p_0 \in \mathbb{R}^+ \tag{37}$$

which maps the region exterior to the contour $\Gamma_c$ in the complex $\xi$-plane to the region $|\eta| > 1$ in the complex $\eta$-plane. Note that, in view of the azimuthal periodicity, the power series in (37) contains only terms associated with integer multiples of $N_p$. By

substituting in (36) the inverse mapping $Q(\eta) = P^{-1}(\eta)$, we obtain

$$\sum_{m=0}^{\infty} b_{p+mN_p}[Q(\eta)]^{p+mN_p} + \sum_{m=1}^{\infty} b_{p-mN_p}[Q^*(\eta)]^{-p+mN_p} \approx \bar{G}_p[Q(\eta)], \quad |\eta| = 1. \tag{38}$$

By straightforward application of the approach in [24], which exploits the asymptotic (large-order) properties of Faber polynomials [36], it can be shown that the summations on the right-hand side of (38) asymptotically approach a *Fourier series* on the unit circle in the complex $\eta$-plane. Hence, truncating to $M_p$ the summations in (38), the point-matching problem is reduced to a truncated-Fourier-series approximation of a known function on the unit circle of an auxiliary complex plane, for which it is well known that *uniform* convergence is guaranteed provided that the sampling points are chosen as *equispaced* on the unit-circle [37]. The desired matching-points in the *physical space* are then readily obtained by inverse mapping to the $\Gamma_c$ contour [cf. (37)] in the auxiliary $\xi$-plane and, finally, to the PEC boundary $r_b(\phi)$ [cf. (35)].

The conformal mapping $Q(\eta)$ can be determined analytically only for a few boundary geometries [24]. For more general geometries, a standard numerical algorithm is based on moment-method-type solution of the related Symm's integral equation [38]. In our implementation, we follow a different numerical approach, based on the approximation of $Q(\eta)$ via a truncated Laurent-series template

$$Q(\eta) \approx \eta \sum_{k=0}^{N_Q} q_k \eta^{-kN_p} \tag{39}$$

where $q_k$ and $k = 0, \ldots, N_Q$ are unknown coefficients to be computed by enforcing that the transformation maps the $|\eta| = 1$ unit-circle onto the $\Gamma_c$ contour in the $\xi$-plane. Recalling (35), this amounts to enforcing that

$$Q\left[\exp\left(j\varphi\right)\right] = \frac{r_e}{r_b(\psi)} \exp\left(j\psi\right) \tag{40a}$$

with the constraint

$$\psi = \arg\left\{Q\left[\exp\left(j\varphi\right)\right]\right\} \tag{40b}$$

where the real variable $\varphi$ parameterizes the unit-circle in the $\eta$-plane. Direct substitution of the constraint (40b) into (40a) would yield a highly nonlinear problem in the unknown coefficients $q_k$. To circumvent this difficulty, we consider $\psi$ as an auxiliary unknown, and follow an augmented Lagrangian approach [39] based on the minimization of the penalty function

$$\mathcal{L} = \sum_{i=1}^{M_s} \left[\frac{r_e}{r_b(\varphi_i)}\right]^2 \times \left\{ \left| \sum_{k=0}^{N_Q} q_k \exp[-j(kN_p - 1)\varphi_i] - \frac{r_e}{r_b(\psi_i)} \exp\left(j\psi_i\right) \right|^2 + 2\Omega \sum_{k=0}^{N_Q} \mathrm{Im}\left\{q_k \exp\left[j\left(1 - kN_p\right)\varphi_i - j\psi_i\right]\right\}^2 \right\} \tag{41}$$

which is the weighted sum of the quadratic residual errors pertaining to the sampled versions of (40b) and (40a), with $\varphi_i$ denoting equispaced samples of $\varphi$, $\psi_i$ denoting unknown samples of $\psi$, and $\Omega$ being an adjustable weight coefficient. The augmented Lagrangian approach consists of minimizing the penalty function in (41) for a sequence of values of the weight coefficient $\Omega$. Each minimization problem is solved via an alternate-descent method [39]. For fixed $\psi_i$ values, a *quadratic* problem is solved in the unknown coefficients $q_k$. Then, for fixed coefficients $q_k$, a sequence of $M_s$ 1-D nonlinear problems is solved with respect to each of the $\psi_i$ (keeping all the other values fixed) via a standard Newton method [39]. The above alternate-minimization scheme is iterated until a suitably defined convergence criterion is satisfied. Concerning the choice of parameters, for the simulation examples presented in Section IV-B, we found that $M_s = 72$ and $N_Q = 24$ provided a satisfactory tradeoff between accuracy and computational burden.

## ACKNOWLEDGMENT

This paper is dedicated to the dear memory of Professor Leo Felsen, mentor and friend. Professor Felsen posed the problem addressed in this paper, and actively participated in the early investigations [15], [16]. The authors would also like to thank the anonymous reviewers for insightful suggestions.

## REFERENCES

[1] Y. G. Sinai, "Dynamical systems with elastic reflections," *Russ. Math. Surv.*, vol. 25, no. 2, pp. 137–189, 1970.
[2] L. A. Bunimovich, "Conditions of stochasticity of two-dimensional billiards," *Chaos*, vol. 1, no. 2, pp. 187–193, Aug. 1991.
[3] A. Wirzba, "Quantum mechanics and semiclassics of hyperbolic n-disk scattering systems," *Phys. Rep.*, vol. 309, no. 1-2, pp. 1–116, Feb. 1999.
[4] T. Kottos, U. Smilansky, J. Fortuny, and G. Nesti, "Chaotic scattering of microwaves," *Radio Sci.*, vol. 34, no. 4, pp. 747–758, Jul.-Aug. 1999.
[5] T. Harayama and P. Gaspard, "Diffusion of particles bouncing on a one-dimensional periodically corrugated floor," *Phys. Rev. E*, vol. 64, Aug. 2001, 036215.
[6] E. Ott, *Chaos in Dynamical Systems*. Cambridge, U.K.: Cambridge Univ. Press, 1993.
[7] A. J. Mackay, "Application of chaos theory to ray tracing in ducts," *IEE Proc. Radar, Sonar Navig.*, vol. 164, no. 6, pp. 298–304, Dec. 1999.
[8] M. V. Berry, "Quantum chaology," *Proc. Roy. Soc. London*, vol. A413, pp. 183–198, 1987.
[9] M. C. Gutzwiller, *Chaos in Classical and Quantum Mechanics*. New York: Springer-Verlag, 1990.
[10] V. Galdi, I. M. Pinto, and L. B. Felsen, "Wave propagation in ray-chaotic enclosures: Paradigms, oddities and examples," *IEEE Antennas Propag. Mag.*, vol. 53, no. 2, pp. 635–644, Feb. 2005.
[11] L. Cappetta, M. Feo, V. Fiumara, V. Pierro, and I. M. Pinto, "Electromagnetic chaos in mode stirred reverberation enclosures," *IEEE Trans. Electromagn. Compat.*, vol. 40, no. 3, pp. 185–192, Aug. 1998.
[12] V. Fiumara, V. Galdi, V. Pierro, and I. M. Pinto, "From mode-stirred enclosures to electromagnetic sinai billiards: Chaotic models of reverberation enclosures," in *Proc. 6th Int. Conf. Electromagn. Adv. Appl. (ICEAA)*, Torino, Italy, Sep. 15–17, 1999, pp. 357–360.
[13] V. Fiumara, V. Galdi, V. Pierro, and I. M. Pinto, "Bouncing ray chaos for smart media," in *Proc. 2000 IEEE Antennas Propag. Int. Symp.*, Salt Lake City, UT, Jul. 16–21, 2000, pp. 682–684.
[14] G. Castaldi, V. Fiumara, V. Galdi, V. Pierro, and I. M. Pinto, "Ray chaos for smart materials," *Atti Fondazione 'Giorgio Ronchi'*, vol. LVIII, no. 3-4, pp. 477–486, May-Jun. 2003.
[15] G. Castaldi, V. Galdi, I. M. Pinto, and L. B. Felsen, "High-frequency wave dynamics of ray-chaotic scatterers," in *Proc. 2004 URSI Int. Symp. Electromag. Theory*, Pisa, Italy, May 23–27, 2004, pp. 948–950.
[16] G. Castaldi, V. Galdi, I. M. Pinto, and L. B. Felsen, "Full-wave analysis of a class of ray-chaotic cylindrical geometries," in *Proc. 2004 IEEE Antennas Propag. Int. Symp.*, Monterey, CA, Jun. 20–26, 2004, vol. 4, pp. 4160–4163.

[17] G. Castaldi, V. Fiumara, V. Galdi, V. Pierro, I. M. Pinto, and L. B. Felsen, "Ray-chaotic footprints in deterministic wave dynamics: A test model with coupled floquet-type and ducted-type mode characteristics," *IEEE Trans. Antennas Propag.*, vol. 53, no. 2, pp. 753–765, Feb. 2005.
[18] J.-F. Kiang, "Scattering properties of circular cylinders with periodical corrugations in the azimuthal direction," *IEEE Trans. Antennas Propag.*, vol. 46, no. 10, pp. 1589–1590, Oct. 1998.
[19] R. B. Greegor, C. G. Parazzoli, J. A. Nielsen, M. A. Thompson, M. H. Tanielian, and D. R. Smith, "Simulation and testing of a graded negative index of refraction lens," *Appl. Phys. Lett.*, vol. 87, no. 9, Aug. 2005, 091114.
[20] T. Driscoll, D. N. Basov, A. F. Starr, P. M. Rye, S. Nemat-Nasser, D. Schurig, and D. R. Smith, "Free-space microwave focusing by a negative-index gradient lens," *Appl. Phys. Lett.*, vol. 88, Feb. 2006, 081101.
[21] D. Schurig, J. J. Mock, B. J. Justice, S. A. Cummer, J. B. Pendry, A. F. Starr, and D. R. Smith, "Metamaterial electromagnetic cloak at microwave frequencies," *Science*, vol. 314, no. 5801, pp. 977–980, Nov. 2006.
[22] R. J. Pieper and A. Nassopoulos, "The eikonal ray equations in optical fibers," *IEEE Trans. Education*, vol. 40, no. 2, pp. 139–143, May 1997.
[23] M. Abramowitz and I. E. Stegun, *Handbook of Mathematical Functions*. New York, NY: Dover, 1972.
[24] A. I. Kleev and A. B. Manenkov, "The convergence of point-matching techniques," *IEEE Trans. Antennas Propag.*, vol. 37, no. 1, pp. 50–54, Jan. 1989.
[25] O. M. Bucci and G. Franceschetti, "On the spatial bandwidth of scattered fields," *IEEE Trans. Antennas Propag.*, vol. 35, no. 12, pp. 1445–1455, Dec. 1987.
[26] J. Van Bladel, *Electromagnetic Fields*. New York: Emisphere, 1985.
[27] C. Jung, C. Mejía-Monasterio, O. Merlo, and T. H. Seligman, "Self-pulsing effect in chaotic scattering," *New J. Phys.*, vol. 6, 2004, 48.
[28] C. Dembowski, B. Dietz, T. Friedrich, H.-D. Gräf, A. Heine, C.Mejía-Monasterio, M. Miski-Oglu, A. Richter, and T. H. Seligman, "First experimental evidence for quantum echoes in scattering systems," *Phys. Rev. Lett.*, vol. 93, no. 13, Sep. 2004, 134102.
[29] H. Lee, C. Jung, and L. E. Reichl, "Scattering echoes in a waveguide with a ripple cavity," *Phys. Rev. B*, vol. 73, no. 19, May 2006, 195315.
[30] L. B. Felsen, "Progressing and oscillatory waves for hybrid synthesis of source excited propagation and diffraction," *IEEE Trans. Antennas Propag.*, vol. 32, no. 8, pp. 775–796, Aug. 1984.
[31] L. Carin and L. B. Felsen, "Wave-oriented data processing for frequency and time domain scattering by nonuniform truncated arrays," *IEEE Antennas Propag. Mag.*, vol. 36, no. 3, pp. 29–43, Jun. 1994.
[32] K. A. Mitchell and J. B. Delos, "A new topological technique for characterizing homoclinic tangles," *Physica D*, vol. 221, no. 2, pp. 170–187, Sep. 2006.
[33] K. M. Frahm and D. L. Shepelyansky, "Quantum localization in rough billiards," *Phys. Rev. Lett.*, vol. 78, no. 8, pp. 1440–1443, Feb. 1997.
[34] S. Wolfram, *The Mathematica Book*. Cambridge, U.K.: Wolfram Media and Cambridge Univ. Press, 2003.
[35] J. L. Walsh, "History of the Riemann mapping theorem," *Am. Math. Mon.*, vol. 80, no. 3, pp. 270–276, Mar. 1973.
[36] J. H. Curtiss, "Faber polynomials and the Faber series," *Amer. Math. Mon.*, vol. 78, no. 6, pp. 577–596, Jun.-Jul. 1971.
[37] D. Jackson, "On the accuracy of trigonometric interpolation," *Trans. Amer. Math. Soc.*, vol. 14, no. 4, pp. 453–461, Oct. 1913.
[38] T. A. Driscoll, "A nonoverlapping domain decomposition method for Symm's equation for conformal mapping," *SIAM J. Numer. Anal.*, vol. 36, no. 3, pp. 922–934, Mar.-May 1999.
[39] R. Fletcher, *Practical Methods of Optimization*. New York: Wiley, 2000.

**Giuseppe Castaldi** was born in Benevento, Italy, in 1968. He received the Laurea degree (*summa cum laude*) in electrical engineering from the "Federico II" University of Naples, Naples, Italy, in 1995, and the and the Ph.D. degree in applied electromagnetics from the University of Salerno, Salerno, Italy, in 1999.

In 2001, he was a Postdoctoral Research fellow at the TNO Physics and Electronics Laboratory, The Hague, The Netherlands. In 2003, he was appointed Assistant Professor of Electromagnetics and joined the Department of Engineering, University of Sannio, Benevento, Italy, where he is currently working. His research interests include electromagnetic chaos, quasi-periodic antenna arrays, applications of neural networks to inverse scattering problems, and field representations in complex environments.

**Vincenzo Galdi** (M'98–SM'04) was born in Salerno, Italy, on July 28, 1970. He received the Laurea degree (*summa cum laude*) in electrical engineering and the Ph.D. degree in applied electromagnetics from the University of Salerno, Salerno, Italy, in 1995 and 1999, respectively.

From April to December 1997, he held a visiting position in the Radio Frequency Division of the European Space Research and Technology Centre (ESTEC-ESA), Noordwijk, The Netherlands. From September 1999 to August 2002, he held a Postdoctoral Research Associate position in the Department of Electrical and Computer Engineering, Boston University, Boston, MA. In November 2002, he was appointed Associate Professor of Electromagnetics, and joined the Department of Engineering at the University of Sannio, Benevento, Italy, where, since February 2005, he has been serving as Associate Chair for Undergraduate Studies in Telecommunication Engineering. In July-August 2006, within the framework of the Laser Interferometer Gravitational-wave Observatory (LIGO) experiment, he held a visiting position at the Massachusetts Institute of Technology, Cambridge, and at the California Institute of Technology, Pasadena. He is the author or coauthor of about 150 papers published in peer-reviewed international journals, books, and conference proceedings. His research interests include analytical and numerical techniques for wave propagation in complex environments, metamaterials, electromagnetic chaos, inverse scattering, and gravitational interferometry.

Dr. Galdi is the recipient of a 2001 International Union of Radio Science (URSI) "Young Scientist Award". He is a member of Sigma Xi, of the LIGO Scientific Collaboration (LSC), of the Italian Electromagnetic Society (SIEM), and of the Italian National Institute of Nuclear Physics (INFN).

**Innocenzo M. Pinto** (M'99–SM'06) was born and educated in Italy.

Winner of national competitions, he was appointed Assistant Professor of Electromagnetics in 1983, Associate Professor in 1987, and Full Professor in 1990. He has been faculty member in the Universities of Naples, Salerno (where he founded and chaired the Ph.D. program in Information Engineering from 1993 to 2001), Catania, and Sannio at Benevento, Italy, where he is currently working. He has visited several research institutions as an invited lecturer, including CERN, KEK, and NIST (former NBS). In 1998, he has been an EU Senior Visiting Scientist at the National Astronomical Observatory, Tokyo, Japan, in connection with the TAMA300 experiment. He authored or coauthored more than 100 technical papers in peer-reviewed international journals. His research interest span from electrophysics to gravitational wave experiments.

Prof. Pinto is a member of the American Physical Society, of the LIGO Scientific Collaboration (LSC), of the Italian National Institute of Nuclear Physics (INFN), and of the Italian Electromagnetic Society (SIEM).